Amplitude and Phase Interaction in Hilbert Demodulation of Vibration Signals: Natural Gear Wear Modeling and Time Tracking for Condition Monitoring

Xavier Laval, Corinne Mailhes, Nadine Martin, Pascal Bellemain, Christian Pachaud

Amplitude and Phase Interaction in Hilbert Demodulation of Vibration Signals: Natural Gear Wear Modeling and Time Tracking for Condition Monitoring

X. Laval[a,*], C. Mailhes[b], N. Martin[a], P. Bellemain[a], C. Pachaud[c]

[a] Univ. Grenoble Alpes, CNRS, Grenoble INP, GIPSA-Lab, 38000 Grenoble, France
[b] Univ. of Toulouse, IRIT/INPT-ENSEEIHT /TéSA, 31000 Toulouse, France
[c] Senior technical consultant, 3 place Sadi Carnot 87350 Panazol, France

---

Abstract

In the context of automatic and preventive condition monitoring of rotating machines, this paper revisits the demodulation process essential for detecting and localizing cracks in gears and bearings. The objective of the paper is to evaluate the performance of the well-known Hilbert demodulation by providing a quantified assessment in terms of signal processing. For this purpose, vibration test signals are simulated guided by the analysis of real-world measurements. The database comes from a natural wear experimentation on a test bench at an industrial scale and without any fault initiation. In the proposed simulated model, the amplitude modulation is designed in a physical approach in order to be able to set up the number of faulty teeth and their location. The impact of a limited spectral bandwidth filtering is quantified not only for the amplitude but also for the phase modulation estimations. The interactions between the amplitude and phase estimations are discussed. A focus is made on the analytic signal ambiguity due to the non-uniqueness of the amplitude estimation. This property induces an original investigation when demodulating the residual generated after a time synchronous averaging. Finally, as the objective is a continuous surveillance of a machine, results are given for a sequence of real-world measurements in order to visualize the fault evolution through the demodulation process.

Keywords: signal processing, envelope, Hilbert demodulation, vibration signal, shock model, residual, time-tracking

---

*Corresponding author
Email address: xavier.laval@gipsa-lab.grenoble-inp.fr (Xavier Laval)

Revised Preprint submitted to Mechanical Systems and Signal Processing May11, 2020

1. Introduction

Advanced signal processing is essential to provide automatic and thorough monitoring of a complex mechanical system to assess its health as part of a condition-based preventive maintenance strategy. It concerns various application domains such as energy (nuclear plants, onshore and offshore wind turbines, marine and tidal turbines, wave energy converters, hydropower plants…), manufacturing and industrial equipment (paper machines, mills, grinders, presses…), transport (railway tracks and vehicles, large-sized construction machines, mining machineries, aircrafts …) or civil engineering (bridges, high-rise buildings, dams…).

Many papers have been published on the spectral analysis of vibrations generated by rotating machines. Among others, B. Randall in 1982 [1] highlighted the importance of identifying modulation sidebands. Three years later, McFadden [2] identified an early fatigue crack in a helicopter gear after looking at the averaged and band-pass filtered signal. Then, a year later, the same author [3] proposed a demodulation process to estimate the amplitude and phase modulations of the same helicopter gear signal. These modulations revealed a small phase lag with minor amplitude modulation in the early stage, and an amplitude falling to near zero with a phase shift of 360° when the crack is advanced and the gear is under load. These studies [1, 2, 3] clearly indicate that a fault investigation should be completed with a demodulation of specific frequency bands to estimate the amplitude, phase or frequency modulations. The demodulation is a very crucial step for the fault localization and characterization.

In this context, an automatic and data-driven sideband demodulation has already been proposed by the authors [4]. The objective of this paper is to assess the performance of that approach by the comparison of the analyses of a proposed vibration signal model and of real-world measurements on a test bench. This paper also compares 2 methods: demodulation on the original signal and on its residual part. The fitting of the proposed model to real-world signals allows a right parametrization of the model and the illustration of the limits of the proposed method by extending the model. As the objective is the continuous surveillance of a system, the measurements are a sequence of signals which convey the evolution of the system state.

Without loss of generality, this paper focuses on a parallel-shaft gear multiplier from a test bench named GOTIX which is described in [5]. Vibration measurements come from a natural wear test at an industrial scale and without any fault initiation.

The multi-estimator method described in [4] and [6] is applied to process both simulated and measured signals. This method provides a detection of all the peaks of a spectrum through a hypothesis test defined in frequency and an automatic clustering of the harmonic families and sidebands. When processing a sequence of measurements over time characterizing the evolution of a system, an automatic tracking method

detailed in [7] links the corresponding peaks from signal to signal to form time-frequency trajectories. These trajectories are a precious help for monitoring a system. This approach has been validated on onshore wind turbines [8] [9] [10] and paper machines [11].

In this approach, the demodulation process needs the estimation of the analytic signal which can be achieved in different ways. The Hilbert transform, a linear operator which produces the orthogonal signal of a real input, is a way to compute the imaginary part of the analytic signal. Another way commonly used in digital communications is called the synchronous or coherent detection and consists of low-pass filtering the output of a multiplier between a complex oscillator at the gearmesh frequency and the signal [12]. As mentioned in the same reference, the Hilbert transform is the only operator that satisfies physical conditions such as amplitude continuity and differentiability, phase independence of scaling and harmonic correspondence. Nevertheless, whatever the estimation is, this complex representation is unique and does not generate a unique decomposition in amplitude and phase which can lead to some ambiguities [14]. In addition, to satisfy these properties, the signal should respect the Bedrosian constraints [13]. Given these conditions and constraints with the use of the Hilbert transform for computing the analytic signal, this paper studies the impact of this choice on the demodulation, in particular the impact of filtering, and deduces some judicious choices for a well-behaved amplitude and phase estimation.

In the faulty gear vibration model proposed, more attention is given to the amplitude modulation. Indeed, this modulation is often modelled as a Fourier series [3] or with a Hanning window [15]. After comparison with the results of the real-world data analysis, this paper considers a model closer to the physics in order to be able to set up physical parameters and to evaluate the detection performance of the demodulation.

This paper presents an in-depth study of the results obtained in [16], in addition to focusing on the ambiguities of the analytic signal. The interactions between amplitude and phase estimations are further analyzed. In addition, given that the gear wear has increased, it is really of interest to show that the demodulation process proposed is now able to detect several failures on specific teeth which actually present spalls. Thus, the proposed model to generate simulated signals is more complex and the performance analysis is thoroughly investigated. All the vibration data used in this paper can be downloaded in [5].

The paper is organized as follows. **Section 2** derives the vibration model of a faulty gearbox with specific simulated models for the frequency and amplitude modulations. In **Section 3**, after a brief recap of the used demodulation already published in [4], the simulated model parameters are set thanks to a comparison with real-world measurement analyses. In **Section 4**, variations of the model parameters give then the possibility to evaluate the demodulation process in both healthy and faulty cases. **Section 5** is a focus on the analytic signal ambiguity according to its definition and its consequences when demodulating a residual signal

generated after time synchronous averaging**. Section 6** comments on the results of the continuous monitoring and the evolution of two natural failures. Finally, **Section 7** draws conclusions and perspectives**.**

2. Simulation model of a faulty gearbox

Aiming to assess the demodulation process of vibratory measurements, the investigation of a model is necessary. A pair of meshing gears is considered at steady-state conditions, that is with a meshing under a constant speed and load. Such a healthy system at nominal speed and at a given load produces a vibration component due to the transmission error of the meshing gears. This component, due to the elastic deformation of the loaded teeth, is load dependent and periodic at the gearmesh frequency with integer harmonics. In addition, geometrical deviations from the ideal tooth profiles contribute to the error transmission also but are not load dependent [17]. Moreover, since there are 2 shafts, one for driving (gear side) and one for braking (pinion side), harmonics at smaller amplitude from the rotations of these shafts can also be found.

In case of a healthy system, a vibration model denoted as $x_{healthy}(t)$ can be written as

$$x_{healthy}(t) = \sum_{h=1}^{N_H} A_h^{mesh}\, sin\left(2\pi h f^{mesh} t + \phi_h^{mesh}\right) + \sum_{g=1}^{N_G} A_g^{gear}\, sin\left(2\pi g f^{gear} t + \phi_g^{gear}\right) + \sum_{p=1}^{N_P} A_p^{pinion}\, sin\left(2\pi p f^{pinion} t + \phi_p^{pinion}\right) + n(t) \quad (1)$$

where, for the gearmesh frequency f^{mesh}, N_H is the number of harmonics, A_h^{mesh} is the amplitude and ϕ_h^{mesh} is the phase of the h^{th} harmonic, for the gear shaft frequency f^{gear}, N_G is the number of harmonics, A_g^{gear} is the amplitude and ϕ_g^{gear} is the phase of the g^{th} harmonic, for the pinion shaft frequency f^{pinion}, N_P is the number of harmonics, A_p^{pinion} is the amplitude and ϕ_p^{pinion} is the phase of the p^{th} harmonic. In addition to these deterministic parts induced mainly by the meshing and shaft rotating forces, the random part of the vibration signal and the non-periodic components $n(t)$ are simply approximated by a stationary Gaussian noise, non-necessarily white.

Let us now assume the occurrence of a local gear fault such as small pits or spalls. This damage gives rise to a local disturbance of the vibration signal. Variations in the meshing force and pressure due to the variation of the tooth surface and profile cause amplitude modulation. These variations create torque transmission errors, which cause speed fluctuations and thus generate frequency modulation as well. The signal is then modulated in amplitude and phase by periodic functions at the rotation frequency of the shaft supporting the faulty gear. Therefore, the vibration model in **Eq. (1)** denoted now as $x_{faulty}(t)$ is modified as

$$x_{faulty}(t) = x_{faulty,fmesh}(t) + \sum_{g=1}^{N_G} A_g^{gear}\, sin\left(2\pi g f^{gear} t + \phi_g^{gear}\right) + \sum_{p=1}^{N_P} A_p^{pinion}\, sin\left(2\pi p f^{pinion} t + \phi_p^{pinion}\right) + n(t), \quad (2)$$

with $x_{faulty,fmesh}(t) = \sum_{h=1}^{N_H} AM_h(t) \sin\left(2\pi \mathrm{h} f^{\mathrm{mesh}} \mathrm{t} + PM_h(t) + \phi_{\mathrm{h}}^{\mathrm{mesh}}\right)$,

where $AM_h(t)$ and $PM_h(t)$ are the amplitude and phase modulations of the h^{th} harmonic of f^{mesh} respectively.

All these vibration sources are transmitted through the structure to the measurement point where the accelerometer is located. As a consequence, a simulated signal denoted as $s_{faulty}(t)$ is obtained through a linear time invariant filter that models this transmission path in the structure

$$s_{faulty}(t) = x_{faulty}(t) * h(t) \quad (3)$$

with $\mathrm{h}(\mathrm{t})$ the impulse response of this filter and $*$ the convolution operator.

The following section will focus on a local fault on one or several gear teeth and consequently on the evolution of $x_{faulty,fmesh}(t)$ in **Eq. (2)**. In this context, the aim is to propose a simulation model for both $AM_h(t)$ and $PM_h(t)$.

2.1. Simulation models of the amplitude modulation

The modelling of the amplitude modulation $AM_h(t)$ is crucial since its choice can lead to different possibilities to fit the reality.

This paper reviews the classical model based on Fourier series and compares it to a second model based on the physics. In both cases, a constraint prevents negative values of $AM_h(t)$. The impact of this constraint is discussed in **Section 5.**

2.1.1.As a Fourier series

As the modulation is a periodic process, $AM_h(t)$ is often represented by discrete Fourier series [2], denoted as $\mathrm{AM}_{\mathrm{h}}^{\mathrm{f}}(t)$

$$AM_h^f(t) = A_h^{mesh}\left(1 + m_h^f(t)\right) \quad (4)$$

$$with\ m_h^f(t) = \sum_{\ell=1}^{L} m_{h,\ell}\, sin\left(2\pi \ell f^{gear} t + \emptyset_{\boldsymbol{h},\ell}\right), \qquad and \quad \left|m_h^f(t)\right| < 1,$$

with L the harmonic number, $m_{h,\ell}$ and $\emptyset_{h,\ell}$ respectively the amplitude modulation index and the random phase of ℓ-order harmonic.

Any periodic function with a finite power can be decomposed in an infinite sum of sines, which argues for the use of this model. Nevertheless, the sinusoidal property of $AM_h^f(t)$ has no direct link with the physics, hence the need of considering high orders.

At some angles, the vibration amplitude of the faulty signal can be lower than the healthy vibration amplitude. As an alternative, the authors in [15] model the fault impact with a Hanning window, the length of which represents the angular duration of the impact.

2.1.2.As a shock series

In order to be closer to physics, another model for $AM_h(t)$ is developed and proposed in this paper. The meshing contact plays the role of the excitation input of the system. To write it simple by considering one degree of freedom only, the equation of a linear motion writes as [18],

$$m\ddot{y}(t) + b\dot{y}(t) + ky(t) = 0, \qquad (5)$$

with $y(t)$ the position of the mass *m*, *b* the damping coefficient and *k* the stiffness. Then the free solution writes as

$$y(t) = Ae^{-\alpha t}\, sin\left(2\pi f_0\sqrt{1-\eta^2}\, t + \phi\right), \qquad (6)$$

with A and ϕ the amplitude and phase respectively, α the damping factor, f_0 the natural frequency and η the damping ratio.

Dealing with vibration signals measured by accelerometers, the second derivative of **Eq. (6)** gives the acceleration generated by the meshing

$$\ddot{y}(t) = -A4\pi^2 f_0^2 e^{-\alpha t}\, sin\left(2\pi f_0\sqrt{1-\eta^2}\, t + \phi + 2arcsin(\eta)\right), \qquad (7)$$

with the notation $f_0 = \frac{1}{2\pi}\sqrt{\frac{k}{m}}$, $\alpha = \frac{b}{2m}$, $\eta = \frac{\alpha}{2\pi f_0} = \frac{b/m}{2\sqrt{k/m}}$.

The aim of this notation is to highlight the role of the stiffness *k* in the following. Indeed, the amplitude writes as $A\frac{k}{m}e^{-\alpha t}$. This equation shows that the amplitude modulation of the instantaneous acceleration is linearly dependent on the stiffness *k i*n the case of one-degree of freedom.

For example, in [27], it is shown that a spall on a gear tooth or a tooth break induce a local drop of the gear stiffness, the profile of which depends a lot on the geometry of the fault. According to **Eq. (7)**, these stiffness drops induce a drop in the amplitude of the instantaneous acceleration. To differentiate cracks and spalls, [28] studies the effect on the transmission error taking into account the load. In [16], the measurements of GOTIX test bench show some amplitude bumps. Inspired by these remarks, and in order to have a generic model, both drops and bumps of the amplitude modulation of the instantaneous acceleration at each gear rotation are considered. Each drop and bump, called a shock, is the response of the system to the fault excitation. The values of these modulation parameters are given by the analysis of the GOTIX measurements in order to be close to the reality. It should be clear that, in this paper, the objective is to generate simulated signals as close as possible to real-world signals in order to evaluate the performance of the signal processing and not to give mechanical interpretation as it is interestingly done for example in [29].

An accelerometer measures the resulting acceleration filtered through the mechanical system. Each input excites the resonance modes of the system, the response of which is the sum of both the forced and free responses of the system at these resonance modes. Thus, let us model $AM_h(t)$ in **Eq. (2)** as a series of *S* shocks, a shock *s* having a positive or negative amplitude and an exponential damping. Let $t_{0,s}$ be the instant of the shock on the first rotation of the gear with regard to a tooth reference.

For a measurement over *R* rotations of the gear, a series of S shocks occurs at each rotation r at instant $t_{r,s} = t_{0,s} + r \times 1/f^{gear}$ with $r = 0, \dots, R$, and $s = 1, \dots, S$. The modal response of the system can be written as

$$x_{faulty,fmesh}(t) = \sum_{h=1}^{N_H} A_h^{mesh}\, sin\left(2\pi h f^{mesh} t + \phi_h^{mesh}\right) + \sum_{r=0}^{R}\sum_{h=1}^{N_H}\sum_{s=1}^{S} A_h^{mesh} m_{h,s} e^{-\alpha_{h,s}(t-t_{r,s})}\, u\left(t - t_{r,s}\right) sin\left(2\pi h f^{mesh}(t - t_{r,s}) + \phi_h^{mesh}\right), \quad (8)$$

where $u(t)$ is the Heaviside step function, $m_{h,s}$ and $\alpha_{h,s}$ the amplitude and damping factor of the shock *s*. More details of this model are given in [18]. The damping factor $\alpha_{h,s}$ is linked to the duration for the stiffness to return to its normal value. Therefore, the amplitude modulation $AM_h(t)$, denoted as $AM_h^{shock}(t)$ for this shock series model, writes

$$AM_h^{shock}(t) = A_h^{mesh}\left(1 + m_h^{shock}(t)\right), \quad (9)$$

$$with\ m_h^{shock}(t) = \sum_{r=0}^{R}\sum_{s=1}^{S} m_{h,s}\, e^{-\alpha_{h,s}(t-t_{r,s})}u\left(t-t_{r,s}\right),\ \ and\quad \left|m_{h,s}(t)\right| < 1.$$

In this paper, it is assumed that the fault does not evolve during the measurement so that the shock parameters, the amplitude $m_{h,s}$ and the damping $\alpha_{h,s}$, are the same at each rotation r. Over one faulty gear rotation and as a function of the rotation angle $\theta = 360 f^{gear} t$ within [0,360] in degrees, the amplitude modulation in **Eq. (9)** is no more *r*-dependent and writes

$$\begin{aligned} AM_h^{shock}(\theta) &= A_h^{mesh}\left(1 + m_{h,s}(\theta)\right), \\ with\ m_h^{shock}(\theta) &= \sum_{s=1}^{S} m_{h,s} e^{-\alpha_{h,s}\,(\theta-\theta_s)/360 f^{gear}} u(\theta-\theta_s), \end{aligned} \qquad (10)$$

with $\theta_s = 360 f^{gear} t_{0,s}$. To characterize each shock from a physical point of view, a direct relation to the relaxation time is given. The relaxation time of a shock modelled by **Eq. (9)** is equal to $1/\alpha_{h,s}$. In this study, the width of a shock is defined as corresponding to three times the relaxation time, i.e., to an attenuation of 26 dB (or an amplitude decrease of 95%). Expressed in pitch, this shock width writes

$$w_\alpha = \frac{3}{\alpha_{h,s}} f^{gear} Z^{gear}, \qquad (11)$$

with Z^{gear} the gear tooth number (see Appendix).

2.2. Simulation model of the phase modulation

If we assume that a local fault is on one gear tooth, $PM_h(t)$ in **Eq. (2)** can be modelled with a sum of C harmonic sine waves of the fundamental f^{gear}, denoted as $PM_h^f(t)$,

$$PM_h^f(t) = \sum_{c=0}^{C} \beta_{h,c}\, sin\left(2\pi c f^{gear} t + \psi_{h,c}\right), \qquad (12)$$

with $\beta_{h,c}$ and $\psi_{h,c}$, respectively the phase modulation index and the phase of the harmonic *c* of the fault frequency f^{gear} and *C* the sine number in the phase modulation. This model has been proposed by [3]. Whatever the value of h , $\beta_{h,0} = 0$. Thus, $C = 0$ induces $PM_h(t) = 0$, a way to represent the case without phase modulation. The frequency modulation rate denoted as FMR_h is defined as

$$FMR_h = \frac{f_{h\,max} - f_{h\,min}}{f_{h\,max} + f_{h\,min}}, \qquad (13)$$

with $f_{h\,max}$ and $f_{h\,min}$ respectively the maximum and minimum frequency of the instantaneous frequency defined from the derivate of $PM_h(t)$. Getting the analytical expression of FMR_h for any value of C is a tricky task. For $C = 1$, the frequency excursion is equal to $2\beta_{h,1}f^{gear}$ and

$$FMR_h = \frac{2\beta_{h,1}f^{gear}}{2hf^{mesh}} = \frac{\beta_{h,1}}{hZ^{gear}}. \quad (14)$$

3. Simulation model identification through demodulation process

After a brief presentation of the analysis and demodulation methods, the aim of this section is to use the models proposed in **Section 2.1** to generate simulated signals with characteristics as close as possible to those of real vibrations measurements.

The reference measurements come from the database of the GOTIX test bench located in GIPSA-lab [5]. The proposed demodulation is applied together with an automatic spectral analysis based on a multi-estimator approach [6]. The analysis of the measurements provides the estimated amplitude and phase modulations, $AM_h(t)$ and $PM_h(t)$ respectively. These estimations are used to generate the simulated signals from the models described in the previous section. In what follows, all amplitude and phase modulations are written as a function of θ in degrees.

3.1. The analysis and demodulation methods

This section briefly recalls the used methods. The spectral analysis is realized thanks to a multi-estimator approach based on Fourier estimators [6] and adapted to vibration signals. It automatically detects peaks, harmonics, sidebands and provides a wide list of advanced features, that can be *a posteriori* associated to kinematic values or labels of the analyzed system [4]. This spectral component detection is based on a two-hypotheses test, as explained in what follows. Let $x(t)$ be a discrete stationary random signal with an estimated power spectral density denoted by $\hat{\gamma}_x(\upsilon)$ and defined as a sum of an unknown signal of interest $s(t)$ and a noise signal $n(t)$,

$$x(t) = s(t) + n(t), \quad (15)$$

where $s(t)$ is a stationary random process, whose estimated power spectral density is denoted by $\hat{\gamma}_s(\upsilon)$, ν being the frequency variable. $n(t)$ is assumed to be a zero mean stationary Gaussian noise, independent of the signal $s(t)$, and with an estimated power spectral density denoted by $\tilde{\gamma}_n(\upsilon)$. This additive noise is not necessarily white. A statistic test based on two hypotheses is defined in the frequency domain,

$$T(\upsilon) = \frac{\hat{\gamma}_x(\upsilon)}{\tilde{\gamma}_n(\upsilon)} \underset{H_1}{\overset{H_0}{\lessgtr}} \mu_{PFA}, \quad (16)$$

with the two hypotheses $H_0: \gamma_x(v) = \gamma_n(v)$, $H_1: \gamma_x(v) = \gamma_s(v) + \gamma_n(v)$, and μ_{PFA} the threshold adjusted from the probability of false alarm of the test.

Adjusting and setting up this test requires answering the following three questions: 1) which kind of estimator should be used for the estimated power spectral density $\hat{\gamma}_x(v)$, 2) how can the noise power spectral density can be estimated and 3) what is the statistics of the test variable $T(v)$ in order to adjust the threshold to a given false alarm probability.

For the estimation of $\hat{\gamma}_x(v)$, one key idea of the approach is to combine the results of several different Fourier estimators according to their complementary properties. Studying the degree of freedom, the spectral leakage percentage, the effective statistical bandwidth and the frequency resolution of various Fourier estimators enable the selection of a set of methods and windows. More details are in [6].

Then, $\hat{\gamma}_x(v)$ is used to estimate $\tilde{\gamma}_n(v)$, as the result of a filtering of $\hat{\gamma}_x(v)$. Previous studies [32] compare various nonlinear filters such as median or morphological filters, but also *n*-path filters that iterate nonlinear estimation and detection for the peak removal. Whatever the choice is, the filter length M should be adjusted according to the spectral window of the Fourier estimator.

The choice of both estimators makes possible the derivation of the distribution of the test statistic under hypothesis H_0. For example, the choice of a median filter for the noise estimation leads to a distribution which can be approximated by a Fisher-Snedecor law $F_{r,rM}$, with parameters r and rM, r being the degree of freedom of the chosen estimator for $\hat{\gamma}_x(v)$ and M being the median filter length. Under hypothesis H_1, the distribution is unknown given that $s(t)$ is unknown. Then, at each spectrum maximum corresponding to a frequency v_{max}, the test is assessed with the *p*-value, defined under H_0 as the probability of having a test value equal or more extreme than the one observed

$$p_0 = Pr[T(v) \geq T(v_{max}) \ / H_0] = \int_{T(v_{max})}^{+\infty} F_{r,rM}(x)dx \tag{17}$$

If the *p*-value is lower than a given threshold corresponding to a probability of false alarm, the corresponding peak potentially belongs to H_1.

Once all peaks belonging to H_1 are detected, a specific algorithm patent-protected [33] and then published in [7] groups all the peaks in harmonic families with their own sidebands. As mentioned in the introduction, this approach has been validated on onshore wind turbines [8] [9] [10] and paper machine [11] in the context of two European projects.

This multi-estimator approach detects all the modulated frequency bands, which can then be demodulated. The used demodulation follows a classical two-steps scheme: first, the signal is band-pass filtered around

the band of interest and second, after a time synchronous averaging, amplitude and phase modulations are calculated through a Hilbert transform. In order to enhance the performance of the final Hilbert transform, sharp transition bands are necessary in the context of real-world signals with a rich spectral content. However, designing such digital filters using conventional methods can be difficult: finite impulse response filters which have a length inversely proportional to the transition width would have a crippling high order and infinite impulse response filters may suffer from a high sensitivity due to their possible instability. To tackle this stability problem, in [4], an innovative band-pass filtering is proposed. It is based on a multi-rate approach [34] to provide a fully automatic solution to design the band-pass filter, whatever the bandwidth constraints are. The objective is to find the stable elliptic filter of the highest order, to benefit from the sharp transition of such filters, while imposing strong constraints to minimize bandwidth ripple. The required elliptic filter order ρ is given by

$$\rho = \frac{K(\tau)K\left(\sqrt{1-\tau_1^2}\right)}{K(\tau_1)K\left(\sqrt{1-\tau^2}\right)}$$

where $K(.)$ represents the complete elliptic integral of the first kind, τ the transition ratio and τ_1 a function of the passband ripple and of the stopband attenuation [35]. Even if for a given order, elliptic filters are optimal in the sense that no other filter has a sharper transition, the strong constraints on the filter specifications may prevent from designing a stable filter. The proposed approach [4] is iterative and uses a multistage implementation of a well-chosen decimation of the signal in order to "zoom" around the passband of interest before designing the filter. The decimation factor is chosen as a compromise between a sufficiently high final sampling frequency and the "relaxing" effect on the required transition band of the filter to be designed: for a given decimation factor *D*, the transition band expressed in normalized frequencies becomes

$$\Delta\tilde{f}_D = \Delta\tilde{f}_0 D,$$

where $\Delta\tilde{f}_0$ is the original required transition band in normalized frequencies. Thus, decimation is a way to transform a highly sensitive filter design problem into a simpler one. Note that the anti-aliasing filter used before decimation is a Butterworth to avoid any distortion in the spectral zoom done by the decimation. Moreover, to perform this decimation whatever the factor *D* required, a multi-stage implementation is proposed.

Even though other demodulation approaches exist, this paper focuses on this Hilbert-based method combined with this efficient band-pass filtering. The aim is to highlight and illustrate the performance of this approach, by looking at the influence of the fault size, the filter band sensitivity, the phase-amplitude correlation, the amplitude rectification of the analytical signal, and the impact of a residual analysis. These

properties are empirically illustrated thanks to the simulated signals inspired from the analysis results on vibration measurements.

3.2. Analysis and demodulation of the measurements

Real-world vibration measurements are performed on the GOTIX bench [5], a test bench which has been designed to produce a database on a natural wearing of a gearbox with two parallel straight gears meshing together. It is important to mention that no fault has been initiated. At the initiation of the test, the gears were new. A gear and a pinion are connected respectively to a driving asynchronous 3-phase motor rotating at 474rpm and a loading DC-generator applying a 200Nm torque on the pinion shaft. The ratio between gear and pinion shaft is 3.8. Then, $f^{gear} = 7.91\ Hz$, $f^{pinion} = 3.8 \times f^{gear} = 30.06\ Hz$ and $f^{mesh} = 450.87\ Hz$. At the time of writing, the database contains over a thousand timestamp folders (more than 6000 hours of rotation), each folder including 18 synchronous measurements such as vibration and electrical data at a sampling frequency $f_s = 25600\ Hz$. The detail of the bench kinematic can be found in the Appendix.

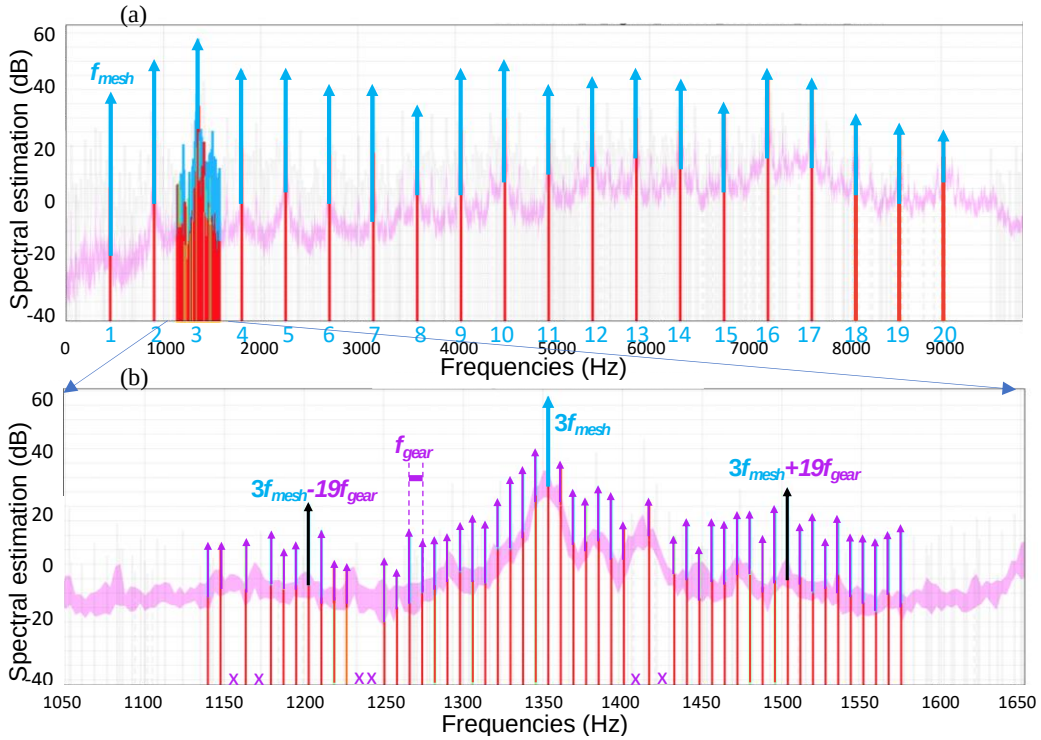

Fig. 1. Detected spectral peaks of a GOTIX measurement at 6240h. (a) The gearmesh harmonics are highlighted with blue arrows. (b) A zoom around **3** $\boldsymbol{f^{mesh}}$, the modulation sidebands are highlighted with purple arrows, undetected sidebands are indicated by a purple cross and a specific focus is made on the 19th sidebands with black arrows.

Applying the multi-estimator approach recalled in **section 3.1**, Fig. 1 shows the detected peaks and harmonic families of a GOTIX measurement at 6240 hours of rotation in the database, that is in the most advanced state of wearing so far. Fig. 1 **(a)** illustrates the main harmonic family due to the gearmesh frequency, each

gearmesh harmonics being modulated by the gear and pinion shafts. For the sake of clarity, only the gear shaft sideband family around the third harmonic is highlighted. Fig. 1 **(b)** presents a zoom around the third gearmesh harmonic with the detected sideband family at the gear shaft frequency.

According to the sensor location, the transmission path can have an impact on the measured vibration and then on the demodulation result. In this study, this transmission path is computed for the measurement considered in Fig. 1. through cepstral liftering [30]. The estimation result is shown in Fig. 2 **(a).** A frequency zoom around the 3rd harmonic in the filtering band considered for the demodulation is shown in Fig. 2 **(b)**. It is clear that, for this harmonic, the transfer function is constant over this narrow filtering band.

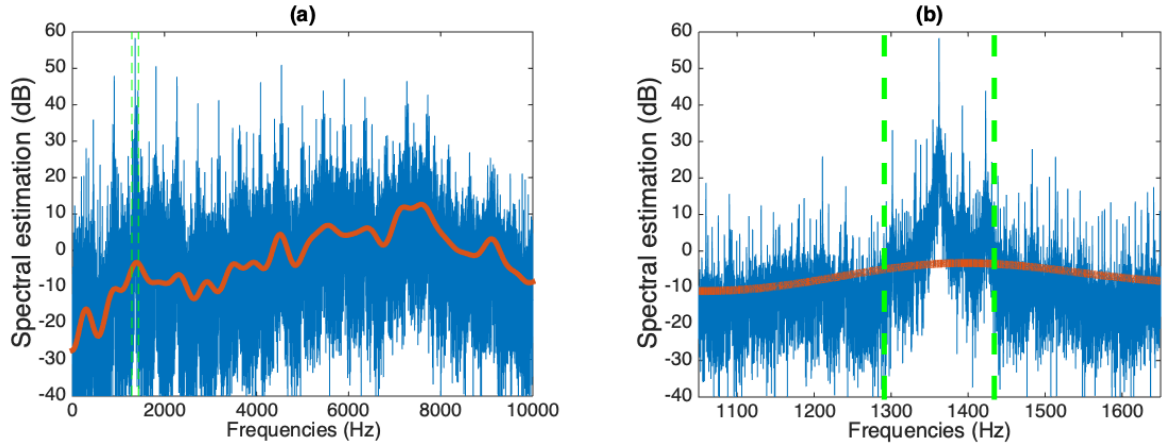

Fig. 2. Estimated transmission path of GOTIX measurement at 6240h. (a) On the entire frequency band. (b) Zoom on the demodulation band around the 3rd harmonic.

Therefore, after the signal analysis, the GOTIX measurements are automatically demodulated by the method recalled in **section 3.1** considering the number of sidebands detected around the 3rd harmonic. Since each gearmesh harmonic is modulated by the same gear frequency, the demodulation band is limited to half the gearmesh frequency on each side, that is to the sidebands $\pm Z^{gear}/2$. However, in the GOTIX case, the assembly design is not optimal. The gear tooth number $Z^{gear} = 57 = 3 \times 19$ and the pinion tooth number $Z^{pinion} = 15 = 3 \times 5$ are not co-prime and have a greatest common divisor equals to 3. It means that 3 tooth family pairs can be present on both the gear and the pinion. One family from the gear (19 teeth) is only meshing with its corresponding family from the pinion (5 teeth). This generates an assembly phase frequency three times lower than in the optimal case when all gear teeth mesh with all the pinion teeth. In the studied case, the sideband structure at the gear frequency has higher energies at frequencies multiple of $19 * f^{gear}$, as can be seen in Fig. 1 **(b)**. These harmonics, with their own sidebands at f^{gear}, are interfering with the modulation pattern.

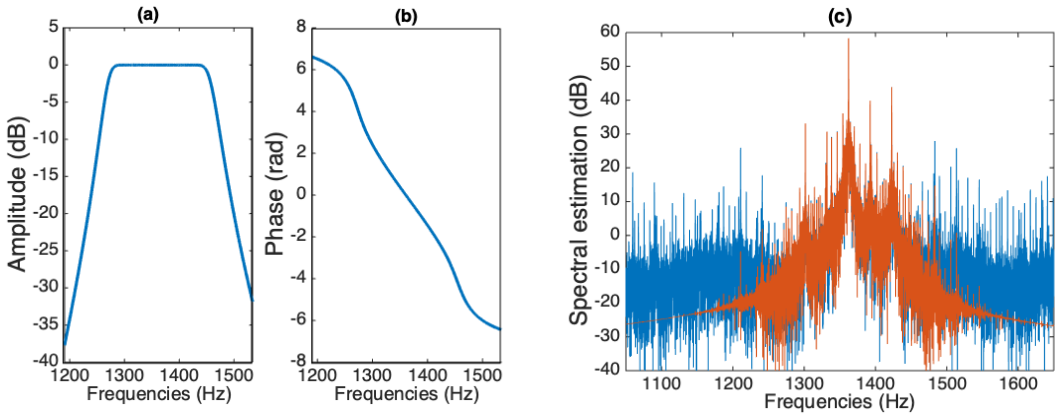

Fig. 3. Design of the filter automatically chosen by the multirate technique. (a) Amplitude response. (b) Phase response. (c) Spectral zoom of the GOTIX measurement at 6240h before filtering (blue) and after filtering (red) around the 3rd harmonic.

Thus, the demodulation band is set to $\pm$ 9 sidebands. Obviously, the fact that this assembly phase family is present indicates that the 3 family pairs are in a different state of wear. This presence could be used as a fault indicator, but it is not the scope of this paper. The demodulation method described in the previous section is then applied in the band [1291 Hz, 1434 Hz] around the 3rd harmonic. Fig. 3 shows the amplitude and phase responses of the elliptic filter found by the method [4] and a spectral zoom before and after filtering. In this particular case, the demodulation band is equal to 143 Hz (corresponding to 0.0054 in normalized frequencies which highlights the extreme narrowness of the required filter band). The algorithm converges in one iteration to an elliptic filter order of 11 and a down sampling factor of 36. The peak-to-peak passband ripple equals 0.005 dB and the stopband attenuation equals 80 dB. These values confirm a challenging design filter.

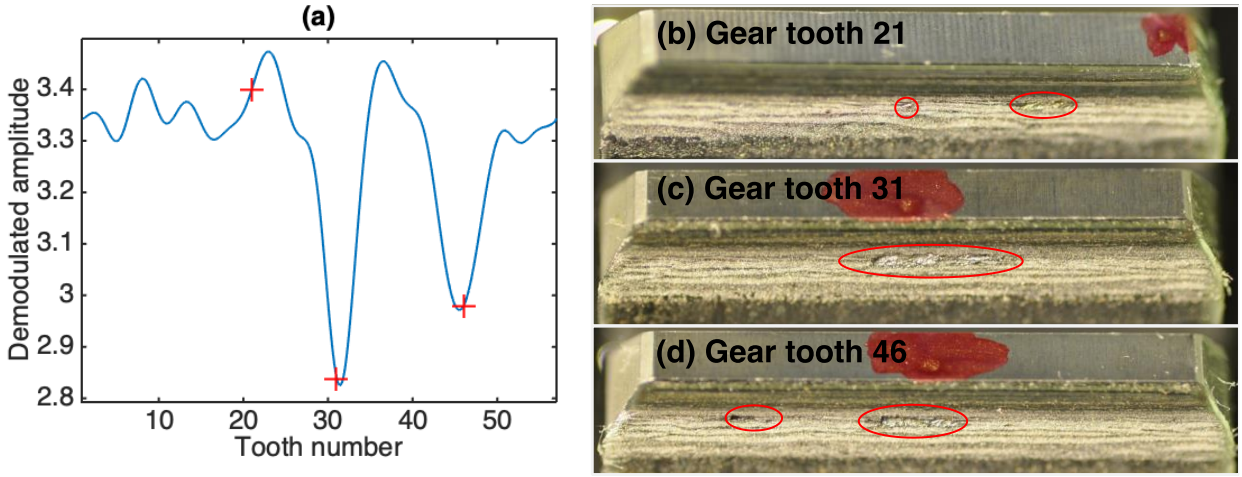

Fig. 4. (a) The estimated amplitude demodulation results $\widehat{AM}_3(\theta)$ of the 3rd harmonic of f^{mesh} of GOTIX measurement at 6240h. (b) Gear tooth 21. (c) Gear tooth 31. (d) Gear tooth 46.

Fig. 4 **(a)** shows the estimation of the amplitude modulation over one gear rotation, $\widehat{AM}_3(\theta)$, for GOTIX measurement at 6240 hours of rotation. This estimated amplitude presents 2 drops in amplitude clearly identifiable and several bumps. A visual inspection on the GOTIX gearbox confirmed that these shocks are

angularly corresponding to the zones of the gear where spall marks are present. The two most severe spall marks have been observed on teeth 31 and 46. Fig. 4 **(c)** and **(d)** show pictures of these teeth whose numbers remarkably correspond to the two minima of $\widehat{AM}_3(\theta)$ in Fig. 4 **(a)**. Other spall marks have been observed, but notably smaller, on tooth 21 in Fig. 4 **(b)** for example.

The spatial sampling δ is the ratio of the gear circumference to the sample number on one gear rotation,

$$\delta = \frac{\pi \, MZ^{gear}}{f_s / f^{gear}} \tag{18}$$

with M the gear module. Numerical values listed in Appendix give $\delta = 0.14\,mm$. This very low sampling period is the result of both relatively low rotation speed and high frequency sampling. Nevertheless, this low sampling does not induce a high resolution. The contact ratio in the GOTIX bench is 1.526. This ratio is the average number of tooth pairs in contact. This value greater than 1 necessarily impacts the confidence interval of the tooth position estimation; this interval is then wider than 1 tooth. But the strongest alteration of the spatial resolution comes from the demodulation process, as shown in **Section 4**.

This preliminary part provides a full spectral estimation of GOTIX measurements, noise line, peaks, harmonic families, sidebands, and demodulated sidebands, from which the simulated signals are generated. For the sake of clarity, only results around the 3nd harmonic are described. The same way can be applied for all harmonics. Note that the different behaviors of all the harmonics are discussed in [33].

3.3. Generation of the simulated signals

Thanks to the analysis of one GOTIX measurement in the previous section, the algorithm provides the amplitude values of the peaks associated to the harmonic families of gear and pinion shafts, and gearmesh. It thus provides the amplitude terms A_h^{mesh}, A_g^{gear}, A_p^{pinion} in **Eq. (2),** which represent the temporal amplitude values of the sine waves that are not corrupted by the noise level. The following discussion will be focused around the 3rd harmonic. Therefore, given the shape of the transmission path estimated in the previous section, the convolution in **Eq. (3)** only impacts the signal of a multiplicative constant amplitude and a linear phase given the operational conditions are constant. This convolution will then have no influence on the demodulation carried on a very narrow frequency band.

The objective now is to find the other parameters of the model so that the quadratic errors between the model and the measurement estimations $\widehat{AM}_h(\theta)$ and $\widehat{PM}_h(\theta)$ are minimal. It is an optimization problem impossible to formulate analytically given that the observation is through an estimation. This error function being scalar-valued and nonlinear, a nonlinear unconstrained optimization problem is formulated and can

be solved thanks to the Nelder-Mead simplex algorithm [26], a simple and fast method for minimizing a function without any derivative.

First a vibration model is simulated with the amplitude modulation $AM_h^f(\theta)$, modelled as the Fourier series described in **Eq. (4)**. The sine number L is found equal to 13. A white noise has been added with a signal-to-noise ratio equivalent to the one estimated on GOTIX measurements and provided by a method based on the autocorrelation function of the signal and published in [20], that is 10 dB. This value has been chosen for all the simulated signals discussed in this paper.

Fig. 5 **(a)** shows the demodulated amplitude $\widehat{AM}_3^f(\theta)$ of the Fourier series model as a function of the gear rotation angle θ. The result is satisfying when comparing with GOTIX demodulation. This result was expected knowing the concept of Fourier series. Nevertheless, this formalism does not give the possibility to link the model parameters to the physical parameters such as the number and localization of faulty teeth. This functionality is very useful to validate the demodulation result; therefore, such a drawback of the Fourier series model was a motivation for a model with physical parameters.

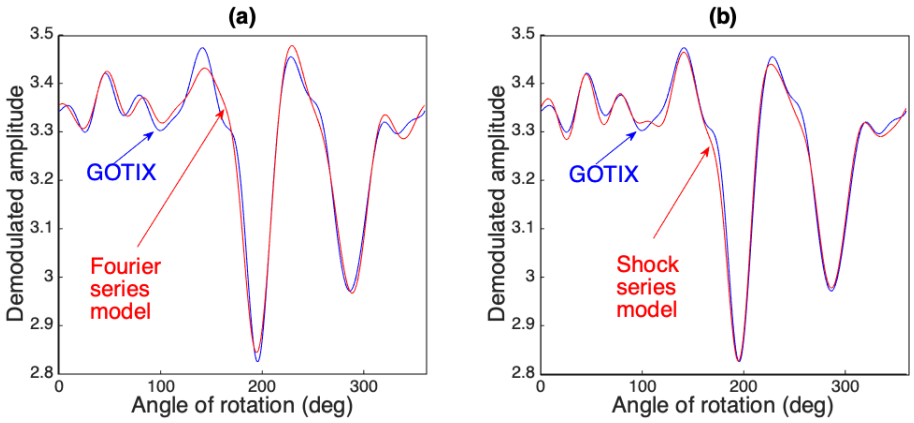

Fig. 5. Comparison of the amplitude demodulation of GOTIX around the 3rd harmonic of f^{mesh}, $\widehat{AM}_3(\theta)$ at 6240h (blue), with 2 models (red). (a) $\widehat{AM}_3^f(\theta)$ from Fourier series model, (b) $\widehat{AM}_3^{shock}(\Theta)$ from shock series model.

For this reason, the amplitude modulation is then modelled as $AM_3^{shock}(\theta)$, the shock series model described in **Eq. (10).** The amplitudes $m_{3,s}$, the shock instants $t_{0,s}$ and the damping factors $\alpha_{3,s}$ are chosen such that the resulting $\widehat{AM}_3^{shock}(\theta)$ of the model demodulation fits the estimated $\widehat{AM}_3(\theta)$ of the GOTIX measurement demodulation using the same optimization process. But, for this model, the parameters to set are of 2 kinds, the amplitudes and the damping factors that are continuous, the shock instants and number that are discrete. The used optimization algorithm does not allow to optimize the discrete parameters, so they are *a priori* set, which is a simple task, and the continuous parameters are estimated thanks to the optimization algorithm. In the end, $S = 12$ shocks have been necessary in order to fit, after demodulation, all variations observed in $\widehat{AM}_3(\theta)$, including the two important drops in amplitude corresponding to the two

minima. Fig. 5 **(b)** shows that the demodulation of the simulated signal fits quite well with GOTIX demodulation. All the drops and bumps of $\widehat{AM}_3(\theta)$ observed in the GOTIX case match this simulation. The identified amplitude modulation, denoted as $AM_3^{fit}(\theta)$, is of interest for the following section due to the physical meaning of its parameters. This model is relevant for studying the impact of demodulation since the parameter setting of the modal response is possible in terms of number, location and damping factors of faulty teeth.

The phase modulation $PM_3(\theta)$ is estimated with the phase model of **Eq. (12),** applying the same optimization algorithm. Fig. 6 shows the result $\widehat{PM}_3^f(\theta)$ with $C = 9$ and $FMR_3 = 0.26\%$. The identified frequency modulation is denoted as $PM_3^{fit}(\theta)$.

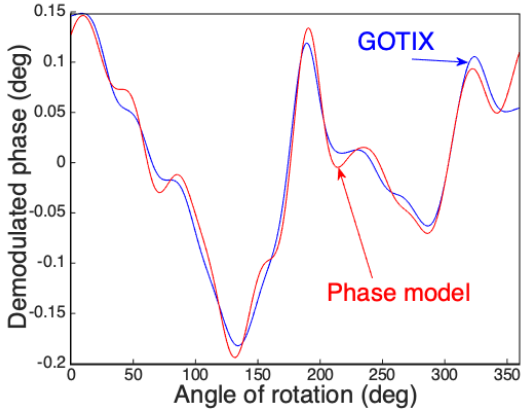

Fig. 6. Comparison of the phase demodulation estimation of GOTIX, $\widehat{PM}_3(\theta)$ at 6240h (blue), with a phase model (red) with $AM_3^{fit}(\theta)$ and $\widehat{PM}_3^{fit}(\theta)$ ($C = 9$, FMR_3 = 0.26%).

4. Fault detection using demodulation

In the previous section, estimation of the model parameters of **Eq. (2)** is done based on real-world signals of the GOTIX test bench, using the proposed model of a shock series for the amplitude modulation given by **Eq. (10)** and the sine model of **Eq. (12)** for the phase modulation. Using these model parameters, simulated signals are generated.

The objective of this section is to show how the efficiency of demodulation in fault detection is impacted by the shock width, strongly dependent on the damping, and the phase modulation, within the context of a very narrow band pass filter linked to the demodulation process**.** This study has already been performed in the case of a mono-carrier model [16] in which only one harmonic of the mesh frequency was considered in the model.

The aim of this section is to consider a more realistic model. The signals simulated are composed of a greater number of harmonics ($N_H = 20$). The characteristics of the amplitude and phase modulation of these signals

are modified from the $AM_h^{fit}(\theta)$ and $PM_h^{fit}(\theta)$ identified in the previous section. The modified parameters are: the width of the main shock (fit value: 5.9 pitches) for the amplitude modulation, the number *C* of sines (fit value: 9) and its FMR_h (fit value: 0.26%) for the phase modulation.

First, in **Section 4.1**, in order to study the effect of the shock width, simulated signals are generated with amplitude modulation only (no phase modulation), with different shock widths w_α in a range close to the one identified on GOTIX signals.

Second, in **Section 4.2**, the simulated signals are modulated in both amplitude and phase, while, in order to study the effect of phase amplitude, different phase model parameters (*C*, FMR_h) are used.

In both cases, as explained in **Section 3.2,** the demodulation of the simulated signals is done around the 3rd harmonic as for the GOTIX measurement. As the filter does not depend on the signal but on its characteristics and the sampling frequency, the filter is exactly the same as in Fig. 3 **(a)** and **(b).** The performance and the limits of the fault detection using demodulation are evaluated thanks to well-chosen criteria. A first criterion of comparison is the classical normalized mean square error ($NMSE$) between the demodulated result and the original model. Two other criteria are introduced to better characterize the drop detection, namely the normalized shock amplitude error (SAE) and the shock position error (SPE), which are defined as follows,

$$SAE = \frac{|A_{min} - \hat{A}_{min}|}{A_{min}} \times 100 \qquad \text{and} \qquad SPE = \left|\theta_s - \hat{\theta}_s\right|, \tag{19}$$

where $A_{min} = A_{mesh} - min\left(AM_h^{shock}(\theta)\right)$ represents the amplitude drop of this shock, $\hat{A}_{min}$ its estimation, and $\hat{\theta}_s$ the estimation of the rotation angle θ_s of the drop (see **Eq. (10)**).

4.1. Amplitude modulation only

As explained above, the aim of this section is to study the effect of shock width on the capacity of the demodulation to detect a fault. Therefore, signals are generated with amplitude modulation only, with different shock widths for the 3rd harmonic. For the sake of clarity, only the shock width of the strongest drop in amplitude around the tooth 31 in Fig. 4 **(a)** is varying. Five values of $\alpha_{3,s}$ are chosen in order to get five angular widths w_α which are $(0.25, 0.5, 1.5, 3.5, 8.5)$, expressed in pitch. No phase modulation is applied to these simulations, referred to as PM0 case.

The demodulation results are presented in Fig. 7 where the comparison is made between the demodulated amplitude and its corresponding original one. In Fig. 7 **(b),** the zoom on the drop with different shock widths shows that this drop is no longer identifiable for the lowest values of w_α, concealed by the other shocks.

Table 1 gives *NMSE*, *SPE* and *SAE* values corresponding to these different shock widths. For the shock widths, $w_\alpha = 0.25$ and 0.5 pitches, the SAE values confirm that the amplitude drop is too small for being correctly detected, due to the influence of other surrounding shocks. For the other shock widths, $w_\alpha = 1.5, 3.5, 8.5$ pitches, the position error SPE increases with w_α, until nearly one gear pitch for $w_\alpha = 8.5$ pitches.

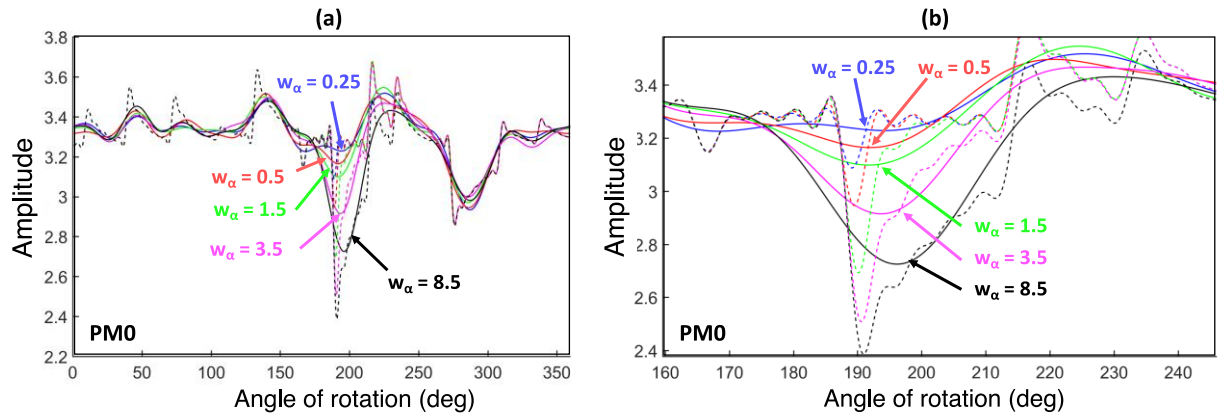

Fig. 7. Influence of model parameters of amplitude modulation without phase modulation. (a) Theoretical models $AM_3^{shock}(\theta)$ with w_α varying from 0.25 to 8.5 pitches for the deepest amplitude drop (dashed lines) and the estimated $\widehat{AM}_3(\theta)$(solid line). (b) Zoom on the main amplitude drop.

These results illustrate the impact of the demodulation as a filtering process, which "smoothes" the output compared to the original model, and introduces an estimation error characterized by the $NMSE$ values of **Table 1**.

Table 1
NMSE, SAE and SPE values of $\widehat{AM}_3(\theta)$ for various shock widths (case of amplitude modulation only).

Indicators of the **amplitude** demodulation	w_α of the amplitude drop model				
	¼ pitch	½ pitch	1.5 pitch	3.5 pitches	8.5 pitches
$NMSE$ (%)	11.1	11.4	13.8	14.3	11.0
SAE (%)	79.1	75.0	66.1	54.1	35.9
SPE (degrees) (pitch)	3.47 (0.55)	2.46 (0.39)	1.57 (0.25)	2.24 (0.35)	5.04 (0.8)

Thus, in order to diagnose a tooth fault properly, obviously, the longer the relaxation time compared to the meshing period, the easier it is to detect. Note that even for the largest shock considered in this study ($w_\alpha = 8.5$), the position error does not impede diagnosis, as it is still below 1 pitch.

4.2. Both amplitude and phase modulations

Let us now consider the case where both amplitude and phase modulations are present. In this section, the simulated signals are modulated in amplitude with different shock widths from 0.25 to 8.5 pitches, including the value estimated in the GOTIX analysis (5.9 pitches). Moreover, to simulate an increasing rate of

frequency modulation, ten couples of (C, FMR_3) are used as detailed in **Table 2**, C being the sine number in the phase modulation and FMR_3 the frequency modulation rate (see **Eqs. (12)** and **(13))**.

Table 2

Values of (C, FMR_3) for the phase model of the simulated signals

	PM0	PM1	PM2	PM3	PM4	PM5	PM6	PM7	PM8	PM9
C	0	1	5	9	1	5	9	1	5	9
FMR_3	0	0.041%	0.22%	0.26%	0.21%	1.1%	1.3%	0.42%	2.19%	2.56%

Note that PM3 corresponds to $PM_3^{fit}(\theta)$ issued from the GOTIX analysis and that PM0 corresponds to the case without phase modulation (amplitude modulation only as in previous section).

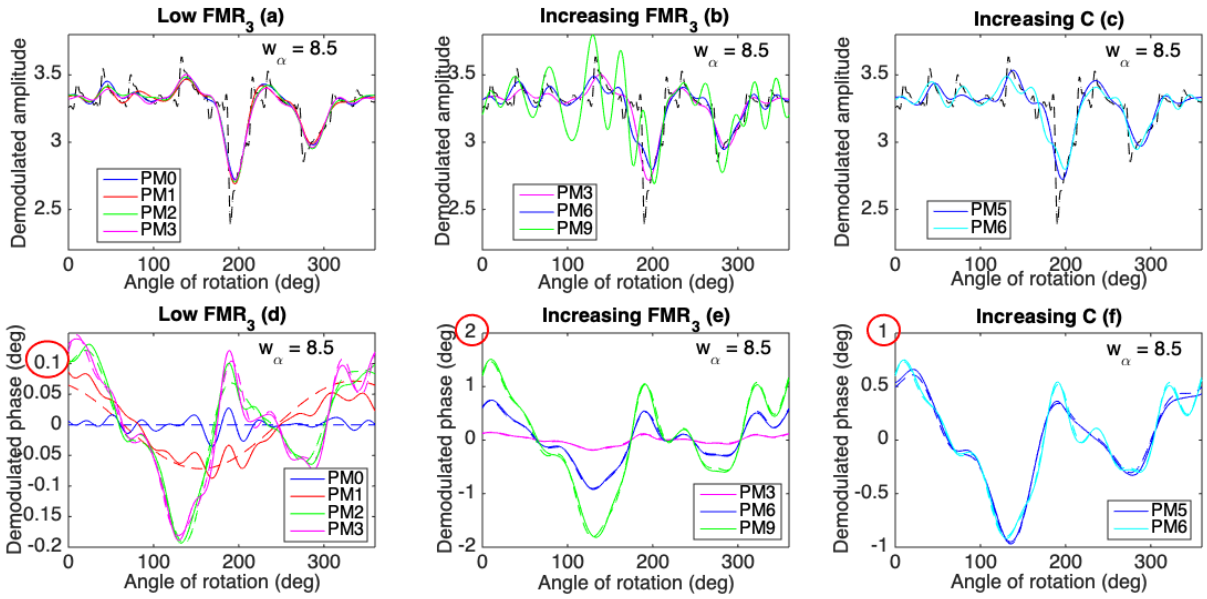

Fig. 8. Impact of phase modulation: theoretical (dashed line) and estimated (solid line). 1st line: $AM_3(\theta)$. 2nd line: $PM_3(\theta)$.1st column: low FMR_3 and variable C. 2nd column: increasing FMR_3 and C=9. 3rd column: increasing C and close middle FMR_3.

The demodulation results in the case of a shock width $w_\alpha = 8.5$ are illustrated in Fig. 8**,** with the demodulated amplitude in Fig. 8 **(a)** to **(c)** and the demodulated phase in Fig. 8 **(d)** to **(f)**.

Regarding amplitude demodulation, in Fig. 8 **(a)** where the FMR_3 is low (<0.26% corresponding to the GOTIX case) and Fig. 8 **(c)** with a higher FMR_3 (around 1.2%), whatever the number C of sine components in the phase model is, the amplitude estimation is mostly impacted by the "smoothing" effect of the demodulation, as already shown in the previous section. However, in Fig. 8 **(b),** showing the results for the highest values of both C and FMR_3, the estimated amplitude modulation becomes useless for PM9 to perform a diagnosis.

This behavior is different for phase demodulation. While theoretical and estimated values are almost identical at intermediate and strong FMR_3 in Fig. 8 **(e)** and Fig. 8 **(f),** the strongest errors appear at low FMR_3. As can be seen in Fig. 8 **(d)** for PM1 and for PM0, the estimated phase modulation is fluctuating with important variations close to the positions of all amplitude bumps and drops. For PM0, the phase should even be equal to zero. The estimated phase in these cases has errors concentrated around the positions of the shocks, especially for the most important one around 200 degrees.

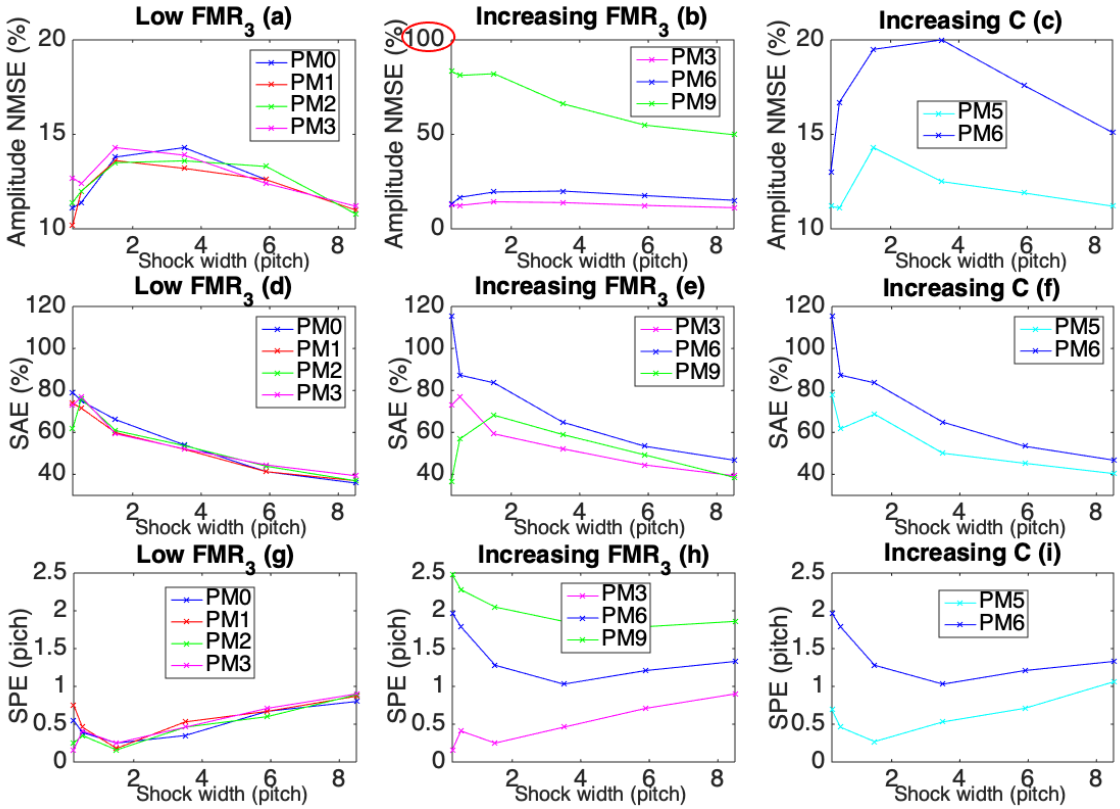

Fig. 9. NMSE, SAE and SPE values for different shock widths and phase modulations.

To highlight the influence of both shock widths and frequency modulation on amplitude demodulation, Fig. **9** presents the amplitude NMSE values (first row of the figure), SAE values (second row) and SPE values (third row) as a function of the shock width, at low frequency modulation rates (PM0 to PM3) in the left column (Fig. **9 (a), (d)** and **(g))**, for increasing frequency modulation rate with the same number of components (PM3, PM6 and PM9) in the middle column (Fig. **9 (b), (e)** and **(f)**) and for an increasing number of components for a comparable FMR_3 in the right column (Fig. **9 (c), (f)** and **(i))**.

At low FMR_3, amplitude NMSE values in Fig. 9 **(a)** are below 15%, whatever the shock width is. Moreover, for any given shock width, the amplitude NMSE values are almost of the same order of magnitude at all FMR_3 from PM0 to PM3. This shows that at low FMR_3, the amplitude demodulation error is mainly due to the demodulation process and its corresponding filtering effect. However, for higher FMR_3, in Fig. 9 **(b),**

the amplitude NMSE is increasing with FMR_3, going up to more than 50% for PM9 (the strongest FMR_3 in our simulations), whatever the shock width is. The same holds in Fig. 9 **(c)** where the amplitude NMSE is increasing with the number of phase components, for a given FMR_3>1%. This highlights the influence of frequency modulation on the amplitude demodulation in the case of a strong frequency modulation.

Fig. 9 **(d),** Fig. 9 **(e)** and Fig. 9 **(f)** illustrate an expected behavior with a decreasing SAE as a function of the shock width: the larger the shock width, the easier the detection. This behavior is observed, whatever the frequency modulation.

Regarding the fault localization, SPE values in Fig. 9 **(g)** are below one pitch, whatever the value of the shock width at all frequency modulation rates from PM0 to PM3. Moreover, as shown in figures Fig. 9 **(a), (d)** and **(g)**, for a given shock width, amplitude NMSE, SAE and SPE values are of the same order of magnitude, regardless of the low modulation rate present in the signal of interest. This confirms that in the case of a low frequency modulation rate, the amplitude demodulation is not influenced by the frequency modulation. However, for a higher frequency modulation or an increasing number of phase components for a given FMR_3>1%, Fig. 9 **(h)** and **(i)** clearly show the influence of frequency modulation on the result of the amplitude demodulation and on the fault localization, with SPE values higher than 1 pitch.

As illustrated in Fig. 8 for a given shock width, the estimation of the phase modulation is also impacted by the amplitude modulation shape. Unlike the amplitude estimation, the greatest impact is at low FMR_3. **Table 3** confirms this behavior through the phase NMSE values. If FMR_3<1%, (PM0 to PM4 and PM7), the phase NMSEs are higher than for the other rates, whatever the number of phase components is. Note that for the clarity, this table is for a shock width $w_a = 8.5$ but the same behavior has been observed for all tested shock widths. Note also that the case without phase modulation, PM0, is not in this table, since it cannot be normalized (the reference being zero).

Table 3
$NMSE$ values of $\widehat{\mathbf{PM_3}}(\theta)$ for $w_a = 8.5$ and different frequency modulation rates.

Phase model	PM1	PM2	PM3	PM4	PM5	PM6	PM7	PM8	PM9
$NMSE$	1.9%	0.8%	0.4%	0.03%	0.02%	0.06%	0.01%	0.02%	0.1%

4.3. Conclusions

As it is well-known, applying a Hilbert demodulation with a strong filtering alters the estimated amplitude and phase modulations. This alteration comes from the removal of distant sidebands, which contain information about both modulations. However, as shown in the two previous sections, even with the observed degradations on the demodulation results, the detection and the localization of the faulty teeth are still possible, except for the cases where phase modulation is too important or when the relaxation time of the modal response is shorter than the meshing period. The dual interpretation in the frequency domain is

easily understandable since it means that the frequency response of the modal response, linked to the inverse of the relaxation time, is greater than the meshing frequency over 2, the limit of the filtering bandwidth.

For a test bench as GOTIX with a $PGCD\left(Z^{gear}, Z^{pinion}\right) > 1$, that is the possible existence of an assembly frequency, when this frequency is not present in the spectrum, the filter is correct given that the band can be equal to $\pm Z^{gear}/2$ sidebands. The presence of this assembly frequency, which in itself is a sign of wear, makes the spectrum more complex as the sidebands are potentially overlapping. Therefore, the filter band should be drastically reduced to $\pm Z^{gear}/2PGCD(Z^{gear}, Z^{pinion})$ sidebands. This section copes with this case where the filter band equals to 0.0554 in normalized frequency. The used multi-rate filtering method succeeded in designing such a filter with a low passband ripple and a high stopband attenuation. This narrow filtering band makes the demodulation performance worse in terms of NMSE, with an aggravation increased for a complex phase modulation. Nevertheless, it allows an interesting fault detection.

This section comments the cross-influence between amplitude and phase modulation. The sidebands out of the filter band contain information from both modulations. Their numbers and energies are troublesome to calculate theoretically. The more components, the wider the spectrum will be. In some particular cases, not illustrated in this paper, the distant sidebands may have higher amplitude values than the first ones. For example, a centrifugal compressor with $Z^{gear} = 375$ teeth was found to have a $\beta_{h,1} = 50$. In these cases, the previous drastic filter will produce much worse results.

In the case of a localized fault, the relaxation time of the modal response is an important characteristic to define the demodulation performance. The shorter it is as compared to the meshing period, the lower is the demodulated amplitude, making it possible to miss a fault. The longer it is, the less accurate is the maximum position, influencing the determination of the faulty tooth.

A high relaxation time coupled with a low amplitude of the modal response (e.g. a mild fault affecting several teeth) may have the same demodulated shape as a severe fault located on one tooth. This limitation of the demodulation regardless of the used method, is due to the non-unity of the amplitude-phase decomposition of the analytic signal as developed in the next section.

5. Demodulation of the residual signal

Some papers, such as [36], [37], report on the demodulation on the residual signal. The residual signal is obtained after applying a time synchronous average with the gearmesh frequency to remove the gearmesh harmonics and enhance the signal to noise ratio. However, in this case, fault detection on the demodulation result has to be done, considering some possible ambiguities, as detailed hereafter.

5.1. The ambiguity of the analytic signal and its polar decomposition

In 1946, Gabor [19] has proposed a definition of the analytic signal $z(t)$ such that the real part equals the analyzed signal denoted here by $x(t)$ and the imaginary part equals the Hilbert transform of this signal

$$z(t) = x(t) + i\mathcal{H}\big(x(t)\big)\,, \tag{20}$$

with $\mathcal{H}(\cdot)$ the Hilbert operator. The Hilbert transform of a real-valued function is a real-valued function. The analytic signal $z(t)$ is complex and unique by definition. As it is the case in the demodulation process, it is often interesting to write $z(t)$ in polar coordinates,

$$z(t) = AM(t)e^{i\Psi(t)}, \tag{21}$$

with AM(t) being the instantaneous amplitude of z(t) and $\Psi(t)$ its instantaneous phase. Unlike representation in Cartesian coordinates of **Eq. (20)**, the representation in polar coordinates of **Eq. (21)** is not unique. It means that the decomposition of the analytic signal in amplitude and phase is not unique as mentioned in former papers [12],[14]. Commonly, the instantaneous amplitude of the analytic signal is defined as

$$AM(t) = \sqrt{x(t)^2 + \mathcal{H}\big(x(t)\big)^2}, \tag{22}$$

and the instantaneous phase as

$$\Psi(t) = arctan\big(\mathcal{H}\big(x(t)\big)/x(t)\big). \tag{23}$$

By doing this, AM(t) is implicitly constrained to be nonnegative. The ambiguity occurs when the amplitude of the signal x(t) is negative at some instants. For example, consider the following signal

$$x(t) = a(t)\,cos(\omega t), \tag{24}$$

where a(t) is a function negative at some instants and ω the pulsation of the signal. The unique corresponding analytic signal $z(t)$ is

$$z(t) = a(t)\,cos(\omega t) + i\,a(t)sin(\omega t) \tag{25}$$

Computing the polar form that is to say the amplitude and phase decomposition using the definitions of **Eq. (22)** and **(23)** gives

$$AM(t) = |a(t)|, \qquad \Psi(t) = \omega t, \tag{26}$$

which are not correct. As written, the complex signal $|a(t)|e^{i\omega t}$ does not equal to **Eq.(25).** Indeed, in this case, the two following decompositions

$$z(t) = a(t)e^{i\omega t} = |a(t)|e^{i\left[\omega t + \frac{1}{2}\pi\left(1 - sgn(a(t))\right)\right]}, \quad (27)$$

are correct (the function $\mathrm{sgn}(.)$ taking ± 1 values depending on the sign of $a(t)$). In the first expression, the instantaneous amplitude is negative, a choice rarely used in practice. In the second expression, the added phase is a function of time to compensate for the rectification of the amplitude constrained to be positive. By convention, this second expression is commonly used. In this second case, whereas the amplitude is rectified at each time the value is negative and aliased around the horizontal time axis, at the same instants, the instantaneous phase presents jumps, and the instantaneous frequency, defined as the derivative of the phase, presents spikes.

5.2. The case of residual signal demodulation

It turns out that this ambiguity problem occurs when demodulating the residual signal. To the best of our knowledge, this problem is not mentioned in the literature. This rectification can lead to a wrong interpretation of both the instantaneous amplitude and the phase. The observed jumps of the phase should not be interpreted as a fault but only as a mathematical artefact. The objective of the following discussion is to illustrate this problem when demodulating a residual signal knowing that an amplitude modulation index lower than 1 is the most frequent case.

The residual signal is obtained by removing the time-synchronous averaged signal at the gearmesh frequency from the vibration signal. This approach is frequently used in vibration analysis and was first proposed by [21]. It is used either to process the obtained time average signal, or to process the residual signal. Details and performances of this method are not the scope of the paper and can be found in many published papers such as [22], [23]. This process is different from the one used in the demodulation process described in **Section 3.1**, where modulation frequency is used instead of the gearmesh frequency.

After removal of the synchronous part, the amplitude modulation of the residual signal denoted in that case by $AM_h^{res}(\theta)$ is

$$AM_h^{res}(\theta) = A_h^{mesh}\, m_h(\theta), \quad (28)$$

given that the gearmesh frequencies and their harmonics have been removed. This removal keeps only the sidebands of interest, as shown in Fig. 10. The residual amplitude $AM_h^{res}(\theta)$ is necessarily lower than $AM_h(\theta)$ and may be close to zero, even negative, particularly in the presence of a fault.

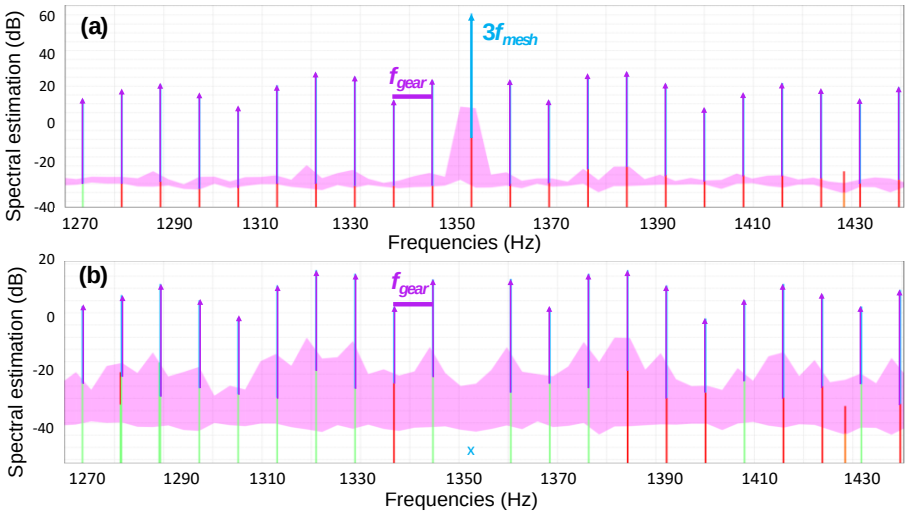

Fig. 10. Spectrum (a) of a simulated signal and (b) of its residual signal around the 3rd harmonic.

Processing the demodulation of the residual signal is usually justified by the strong amplitude influence of the tooth meshing vibration. Indeed, these vibrations are not only important but also positively correlated to their modulation sidebands [25]. However, in that case, it is worth pointing out the ambiguity brought by the amplitude and phase decomposition of the Hilbert-based demodulation, as detailed in the previous **section 5.1.**

Fig. 11 **(a)** compares both the estimated amplitude of a simulated signal and its residual signal which should almost be the same, up to an additive constant. For the sake of clarity, the simulated signal is simply designed with only one shock in the amplitude and, what is very important to notice, without phase. $\widehat{\mathrm{AM}}_3^{\mathrm{res}}(\theta)$ is clearly rectified at the shock location in order to respect the positivity constraint. Without this constraint, the estimation would have been as a translation of $\widehat{\mathrm{AM}}_3^{\mathrm{res}}(\theta)$, this expected curve is represented by a dashed curve in Fig. 11 **(a).**

This amplitude rectification has also a strong impact on the phase, knowing that the simulated signal has no phase modulation. As shown in Fig. 11 **(b),** phase jumps occur at each amplitude rectification. As explained above, these phase jumps of value π are equivalent to a negative sign and thus preserve the unicity of the analytic signal. Furthermore, the unwrapping of the phase becomes trickier, and leads to a drift. The positions of the phase jumps are clearly visible in the instantaneous frequency, derivative of the phase, and represented in Fig. 11 **(c)**. The reading of the phase or instantaneous frequency can incorrectly conclude to the presence of more than one fault.

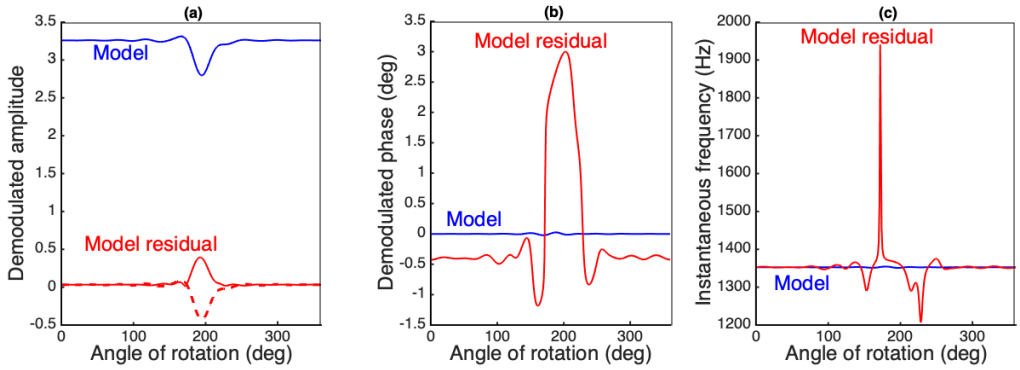

Fig. 11. Comparison of the demodulation of a model (blue) for a one-shock model without phase modulation (PM0) with its residual (red). (a) $\widehat{AM}_3(\theta)$ and $\widehat{AM}_3^{res}(\theta)$. The dashed red line is a translation of the model to be at the same level as the residual, for comparison purpose. (b) $\widehat{PM}_3(\theta)$ and $\widehat{\mathrm{PM}}_3^{\mathrm{res}}(\theta)$. (c): Corresponding instantaneous frequencies.

Consequently, this amplitude rectification and these phase jumps can clearly induce a wrong interpretation of the demodulation functions. In particular, it might be tempting to conclude that the phase is more meaningful than the amplitude. However, in this example, the strong impacts in the phase come from a processing artefact when demodulating the residual.

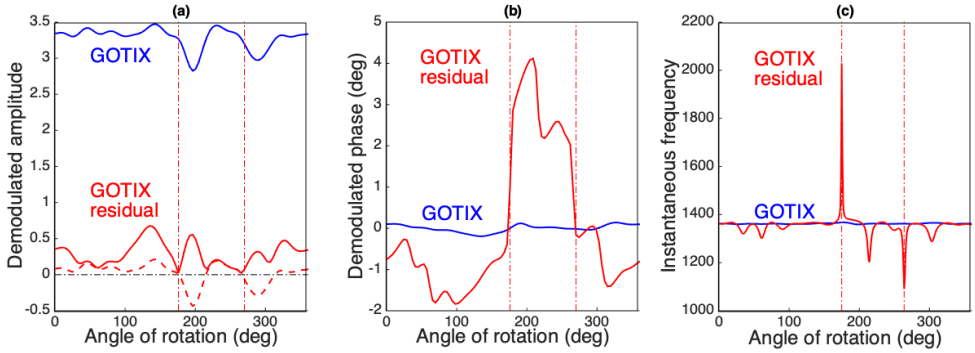

Fig. 12. Comparison of the demodulation of GOTIX measurement (blue) at 6240h and around the 3rd harmonic and its residual (red). (a) $\widehat{AM}_3(\theta)$, $\widehat{\mathrm{AM}}_3^{\mathrm{res}}(\theta)$ and $\left(\widehat{AM}_3(\theta) - A_3^{mesh}\right)$ (dashed red) (b) $\widehat{PM}_3(\theta)$ and $\widehat{PM}_3^{res}(\theta)$. (c) Corresponding instantaneous frequencies.

This problem of the residual signal demodulation, highlighted in Fig. 11 on a simulated signal, has been often observed when processing real-word signals with or without time synchronous averaging. Indeed, when comparing both results of demodulation applied directly on the GOTIX measurement or on its residual signal, the rectification of the residual amplitude estimation is clearly visible, as shown in Fig. 12 **(a)** where the dashed red curve corresponds to what should be obtained. The difference in the phase estimations or instantaneous frequencies in Fig. 12 **(b)** and **(c)** is really striking.

The ambiguity inherent to the demodulation process when applied to the residual signal is explained in this section and illustrated on simulated as well as real signals. This leads us to conclude that, to avoid false detection, the demodulation should be applied on the signal and not on the residual signal.

6. Surveillance: results of a continuous monitoring

The interest of demodulation is not only for analyzing one signal but also for a continuous preventive surveillance of a system. In a continuous monitoring, successive signals are analyzed by the same approach described in **section 3.1**. A dedicated time-frequency tracking over all previous time stamps [7] builds trajectories of peak, harmonic and sideband families that generate continuous system health indicators. This tracking is of interest to evaluate the evolution of the system health.

In that context, the GOTIX test bench provides a sequence of measurements regularly updated with new ones. The objective of this section is to show the demodulation results of a sequence of 427 measurements during the last 3200 hours of rotation. At the beginning of this sequence, the GOTIX bench has already been running for over 3000 hours, but with a change in an operational parameter, a decrease in the braking torque. Hence the choice to consider only the signals after this change. This means that the gear on the first analyzed signals in Fig. 13 was already slightly worn. Each signal is synchronized thanks to a top-tour connected to the gear. Thus, each signal begins at the same gear angular position, and the amplitude modulations correspond to one rotation starting always from the same point.

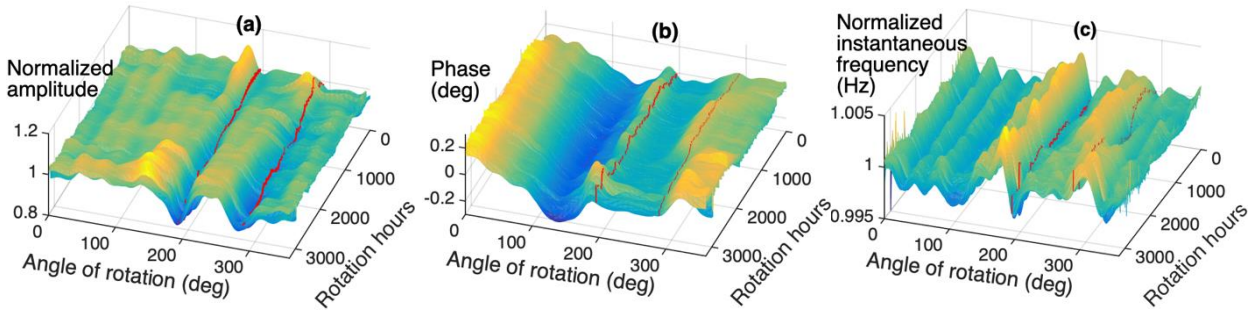

Fig. 13. Monitoring of GOTIX based on the estimated demodulations around the 3rd harmonic between 0 and 3200h. (a) Normalized amplitude modulations $\widehat{AM}_3(\theta)$. (b) $\widehat{PM}_3(\theta)$. (c) Instantaneous frequency. All measurements were synchronized with reference to a top-tour encoder. The red lines show the 2 main worn teeth, gear teeth 31 and 46.

The used method is able to automatically compute the demodulation of the measurements in all the sequence of measurements The demodulation is done around the third harmonic for each signal. Fig. 13 shows the 3D representations of the amplitude in **(a)**, of the phase in **(b)** and of the instantaneous frequency obtained by derivative of the phase in **(c)**. Thanks to synchronization and constant operating conditions, these functions show a very continuous evolution. The two red lines in the 3 representations track the position of tooth 31 and tooth 46 respectively. In Fig. 13 **(a)**, the variations of $\widehat{AM}_h(\theta)$ shows a bump just before tooth 31 at the beginning of the test. This bump disappears after a few hours of rotation. Then, an increasingly large drop in amplitude is clearly initiated at tooth 31. At tooth 46, a drop in amplitude occurs after about 1000 hours of rotation only. In contrast, in Fig. 13 **(b)** and **(c),** the trends of $\widehat{PM}_h(\theta)$ and of the instantaneous

frequency are not as easily interpreted as those of $\widehat{AM}_h(\theta)$. Nevertheless, it is remarkable that the two areas around teeth 31 and 46 are the only ones that show significant variations during the test.

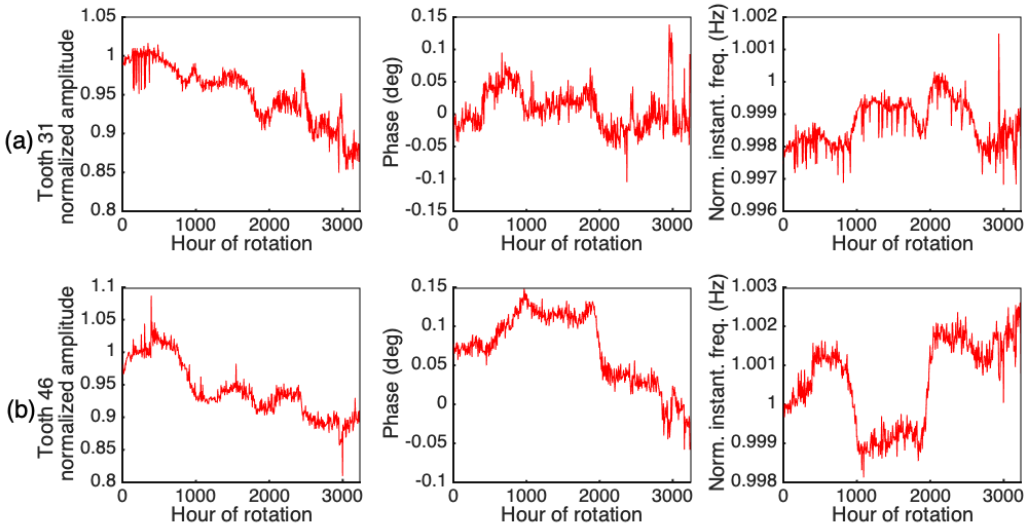

Fig. 14. Cross-sections in **Fig. 13** over 3200 hours of rotation**.** (a) At tooth 31. (b) At tooth 46.

Cross-sections of these 3 estimators, amplitude, phase and instantaneous frequency, represented in Fig. 14 at two positions, teeth 31 and 46, illustrate clearly a noticeable decreasing trend in the amplitude for these two faulty teeth.

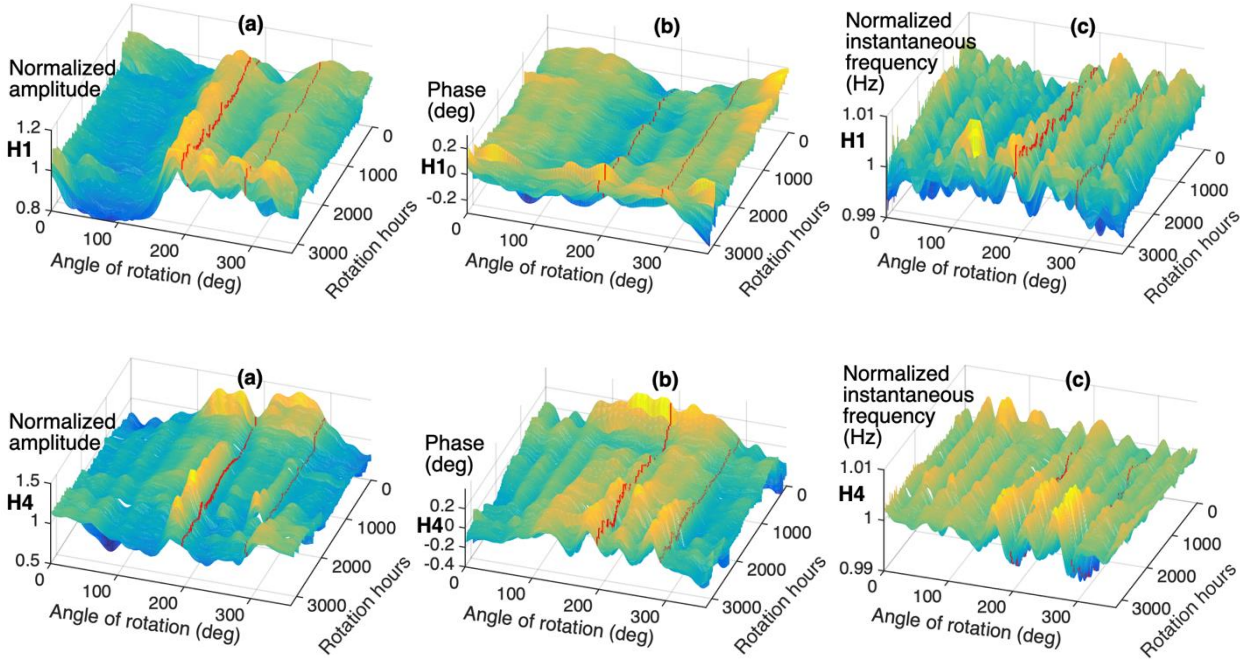

Fig. 15. Tracking of GOTIX measurements between 3012h and 6245h through demodulation around 1st (top) and 4th (bottom) harmonics. (a) Normalized amplitude modulations $\widehat{AM}_h(\theta)$. (b) Phase modulation $\widehat{PM}_h(\theta)$. (c) Instantaneous frequency (derivative of $\widehat{PM}_h(\theta)$). All measurements were synchronized with reference to a top-tour encoder. The red lines show the 2 main wear teeth, gear teeth 31 and 46.

The demodulation amplitudes decrease consistently over time, featuring an aggravation of the spalls. Thus, the choice of the 3rd harmonic for the demodulation is *a posteriori* justified by the good results on its long-term monitoring. In order to compare with other harmonics, the monitoring is performed on harmonics 1 and 4, as shown in Fig. 15.

This extended monitoring also shows signs of faults around teeth 31 and 46, in particular with the appearance of shocks in the amplitude modulation. However, the trends are not as clear as around the 3rd harmonic, and these shocks are now positive. In order to increase the reliability of the detection in a continuous automatic monitoring context, the demodulation should thus be performed around several different harmonics.

7. Conclusions

In the context of automated monitoring for preventive maintenance purposes, this paper explores the steps of demodulation or so-called 'envelope analysis', an essential process for an earlier detection and localization of faults in the analysis of vibrations generated by rotating machines. This paper focuses on the well-known and often used method based on the Hilbert transform. The main objective is to quantify the performance of the demodulation process by comparing analyses of real-world vibration measurements and models. Results are computed from the database of a natural wear test of a parallel straight-teeth multiplier on the GOTIX test bench. At the test beginning, the multiplier was a new-build gear without fault initiation. This wear test is carried out at a point where several spalls of different wear degrees are observed.

A performance assessment requires simulated signals and then a model is used for this purpose only. A shock series function models the amplitude modulation. The model parameters are set thanks to an experimental fitting with the measurement analysis. Such a parametrization is expressed directly in terms of physical parameters. These parameters are then tuned to simulate a variety of failures in terms of number of faulty teeth, their position, and the severity of their degradation. The phase modulation is modeled with a sum of harmonic sine waves.

The main trouble in the Hilbert demodulation is the filter bandwidth around the carrier frequency; this bandwidth could not be wide enough due to aliasing with the other harmonics. The performance is discussed in the case of a strong filtering, which necessarily impacts the modulation estimation. Nevertheless, the results show that a detection and localization of the failure are still possible except for the cases where phase modulation is too important or when the relaxation time of the modal response is shorter than the meshing period. In the paper context, the fault detection based only on the phase is not performing, whereas the amplitude modulation is able to highlight the presence of several faults.

This paper comes back to the non-unicity of the amplitude and phase decomposition of the analytic signal. A demodulation process based on Hilbert transform needs a polar transform of the analytic signal. This decomposition being not unique, it can lead to misinterpretation when the amplitude modulation index is lower than the unity. An example is illustrated when demodulating a residual signal obtained after the removal of all gearmesh harmonics.

In the end, a sequence of measurements is automatically demodulated for a continuous preventive surveillance of the GOTIX bench. The 3D or 2D representation of the amplitude and phase modulations may be of a great help for detecting the faulty tooth positions. Further works are in progress for defining new condition monitoring features from these representations.

Appendix. GOTIX test bench

- Driving three-phase asynchronous motor Leroy-Somer P280 S-8, 55 kW. $f^{gear} = 474\ rpm$
- Braking DC generator Leroy-Somer 54.3 kW, commanded by a Leroy-Somer DMV 2342 inverter. The motor is powered either by Altivar 66 inverter. Parallel straight teeth in case-hardened steel.
- Module M=2.5 mm, Tooth number: $Z^{gear} = 57$, $Z^{pinion} = 15$
- OROS acquisition system, $f_s = 25600\ Hz$, data length 10s, 18 synchronous channels: 6 accelerometers, 3 phase current & voltage sensors, 1 torquemeter, 1 tachometer and 2 optical encoders with top-tour.

See the synoptic view in Fig. 16. Further details can be found in GOTIX website [5] where data used in this paper can also be downloaded. 0 to 3200 hours of rotation correspond to 3012h and 6245h timestamps.

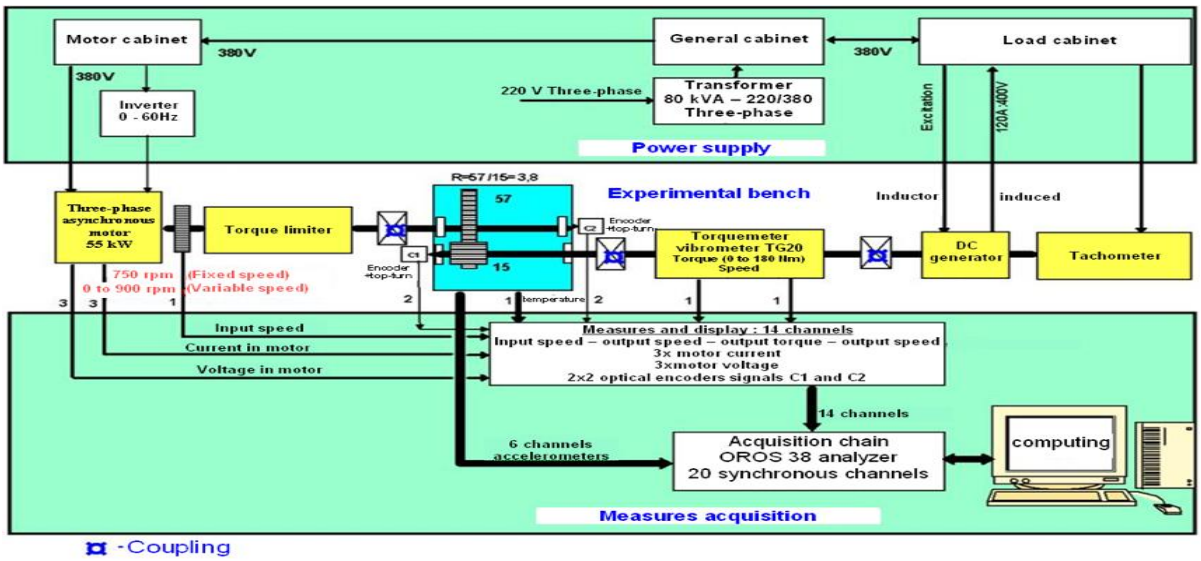

Fig. 16. Synoptic view of the test bench GOTIX.

References

1. R. B. Randall, A new method of modelling gear faults. Trans. ASME, J. Mech. Des., 104 (1982) 259-267. https://dx.doi.org/10.1115/1.3256334
2. P.D. McFadden, J.D. Smith, A Signal Processing Technique for Detecting Local Defects in a Gear from the Signal Average of the Vibration, Proceedings of the Institution of Mechanical Engineers, Part C, 199 (43) 287-292.

   https://dx.doi.org/10.1243/PIME_PROC_1985_199_125_02
3. P.D. McFadden, Detecting Fatigue Cracks in Gears by Amplitude and Phase Demodulation of the Meshing Vibration, Journal of Vibration, Acoustics, Stress, and Reliability in Design, 108 (1986) 165-170. https://dx.doi.org/10.1115/1.3269317
4. M. Firla, Z.-Y. Li, N. Martin, C. Pachaud, T. Barszcz, Automatic Characteristic Frequency Association and All-Sidebands Demodulation for Detection of a Bearing Fault of a Wind Turbine Test Rig, MSSP, 80 (2016) 335-348. https://doi.org/10.1016/j.ymssp.2016.04.036
5. GOTIX, Characterization of defects on electrically driven mechanical systems. http://www.gipsa-lab.grenoble-inp.fr/projet/gotix/gearwear.html (accessed 2019).
6. N. Martin, C. Mailhes, Automatic Data-Driven Spectral Analysis Based on a Multi-Estimator Approach, Signal processing, 146 (2018) 112-125. https://doi.org/10.1016/j.sigpro.2017.12.024
7. T. Gerber, N. Martin, C. Mailhes, Time-frequency Tracking of Spectral Structures Estimated by a Data-driven Method, IEEE Trans. on Industrial Electronics, Special Session, 52 (10) (2015) 6616-6626. https://dx.doi.org/10.1109/TIE.2015.2458781
8. N. Martin, Invited Keynote Address, KAStrion project: a new concept for the condition monitoring of wind turbines, CM-MFPT 2015, UK, 9-11 June 2015. https://hal.archives-ouvertes.fr/hal-01166347
9. Z.-Y. Li, T. Gerber, M. Firla, P. Bellemain, N. Martin, C. Mailhes, AStrion strategy: from acquisition to diagnosis. Application to wind turbine monitoring. International Journal of Condition Monitoring, 6 (2) (2016) 47-54.

   https://dx.doi.org/10.1784/204764216819375267
10. X. Laval, G. Song, Z.-Y. Li, P. Bellemain, M. Lefray, N. Martin, A. Lebranchu, C. Mailhes, Invited Keynote Address, AStrion assets for the detection of a main bearing failure in an onshore wind turbine, CM-MFPT 2016, France, 10-12 October 2016. https://hal.archives-ouvertes.fr/hal-01399027
11. M. Eltabach, S. Sieg-Zieba, G. Song, Z.-Y. Li, P. Bellemain, N. Martin, Vibration condition monitoring in a paper industrial plant: Supreme project, CM 2016 and MFPT 2016. Paris, France, 10-12 October 2016. https://hal.archives-ouvertes.fr/hal-01399036
12. D. Vakman, On the Analytic Signal, the Teager-Kaiser Energy Algorithm, and Other Methods for Defining Amplitude and Frequency, IEEE Trans. on Signal Processing, 44 (4) (1996) 791-797. https://dx.doi.org/10.1109/78.492532
13. E. Bedrosian, A product theorem for Hilbert transforms, Proceedings of the IEEE, 51 (5) (1963) 868-869. https://dx.doi.org/10.1109/PROC.1963.2308
14. L. Cohen, P. Loughlin, D. Vakman, On an ambiguity in the definition of the amplitude and phase of a signal, Signal Processing 79 (1999) 301-307. https://doi.org/10.1016/S0165-1684(99)00103-6
15. D.Abboud, J. Antoni, S. Sieg-Zieba, M. Eltabach, Envelope analysis of rotating machine vibrations in variable speed conditions: A comprehensible treatment, MSSP, 84 (2) (2017) 200-226. https://doi.org/10.1016/j.ymssp.2016.06.033
16. X. Laval, N. Martin, P. Bellemain, Z.-Y. Li, C. Mailhes, C. Pachaud, Vibration response demodulation, shock model and time tracking. CM 2018 and MFPT 2018. Nottingham, UK, 10-12 September 2018
17. R.B. Randall, Vibration-based Condition Monitoring, J. Wiley & Sons Ed., 2011
18. N. Martin, P. Jaussaud, F. Combet, Close shocks detection using time-frequency Prony Modelling, MSSP 18 (2) (2004) 235-261. https://doi.org/10.1016/j.ymssp.2004.04.004
19. D. Gabor, Theory of communication, IEEE J. Comm, Eng. 93 (1946) 429-457
20. G. Song, Z.-Y. Li, P. Bellemain, N. Martin, C. Mailhes, AStrion data validation of non-stationary wind turbine signals, CM-MFPT 2015, UK, June 9-11, 2015. https://hal.archives-ouvertes.fr/hal-01166419
21. P. D. McFadden, J. D. Smith, A signal processing technique for detecting local defects in gear from the signal average of the vibration, Proc. In. Mech, Eng.(1985) 287-292.
22. E. Bechhoefer, M.Kingsley, A review of time synchronous average algorithms, Annual Conference of the Prognostics and Health Management Society, (2009), 1–10.

http://72.27.231.73/sites/phmsociety.org/files/phm_submission/2009/phmc_09_5.pdf

23. P. D. McFadden, A revised model for the extraction of periodic waveforms by time domain averaging, Mech. Syst. Signal Process.1 (1) (1987) 83–95. http://dx.doi.org/10.1016/0888-3270(87)90085-9
24. G. Krishnappa, Gear fault detection parameters development based on modulation techniques, Int. Congress on Sound and Vibration, ICSV, Adelaide, South Australia, December 15-18, 1997.
25. F. Combet, L. Gelman, Novel adaptation of the demodulation technology for gear damage detection to variable amplitudes of mesh harmonics, MSSP 25 (2011) 839-845. https://doi.org/10.1016/j.ymssp.2010.07.008
26. J. A. Nelder and R. Mead, A simplex method for function minimization, Computer Journal 7 (1965), 308–313. https://doi.org/10.1093/comjnl/7.4.308
27. F. Chaari, W. Baccar, M. S. Abbes, M.Haddar, Effect of spalling or tooth breakage on gearmesh stiffness and dynamic response of a one-stage spur gear transmission, European Journal of Mechanics A/Solids 27 (2008) 691–705. https://doi.org/10.1016/j.euromechsol.2007.11.005
28. H. Endo, R. B. Randall, C. Gosselin, Differential diagnosis of spall vs. cracks in the gear tooth fillet region: Experimental validation, MSSP 23 (2009) 636-651.
29. E. Hubert, P. Borghesani, R. B. Randall, M. El-Badaoui, Challenging the traditional model of gear vibration signals, Survishno conference, Lyon, 8-10 July 2019.
30. R. B. Randall, W. A. Smith, New cepstral techniques for operational modal analysis. First World Congress on Condition Monitoring, London, UK, June 13-16, 2017.
31. X. Laval, N. Martin, P. Bellemain, C. Mailhes, Detection and localization of a gear fault using automatic continuous monitoring of the modulation functions, 2nd World Conference on Condition Monitoring, WCCM 2019, Singapore, 2-5 December 2019.
32. M. Durnerin, A strategy for the interpretation in spectral analysis, detection and characterization of spectrum components (in French), Ph.D. thesis, INPT, Grenoble, France (1999), available on https://tel.archives-ouvertes.fr/tel-00789941/.
33. N. Martin, C. Mailhes, and T. Gerber, Anomaly detection system, Patent no. FR N13/53860, 2013.
34. L. Milic, T. Saramaki, R. Bregovic, Multirate filters: an overview. APCCAS 2006 - 2006 IEEE Asia Pacific Conference on Circuits and Systems, Singapore, 2006, pp. 912-915.
35. L. R. Rabiner, B. Gold, Theory and application of digital signal processing. Prentice Hall Inc., Englewood Cliffs, N. J., 1975.
36. W. Wang, Early detection of gear tooth cracking using the resonance demodulation technique, MSSP (2001) 15(5), 887-903. https://doi.org/10.0.3.238/mssp.2001.1416
37. Y. Marnissi, D. Abboud, M. Elbadaoui, Vibration-based health monitoring methodology for helicopter gearboxes, CM 2018 and MFPT 2018. Nottingham, UK, 10-12 September 2018